

Contract No.:

This manuscript has been authored by Savannah River Nuclear Solutions (SRNS), LLC under Contract No. DE-AC09-08SR22470 with the U.S. Department of Energy (DOE) Office of Environmental Management (EM).

Disclaimer:

The United States Government retains and the publisher, by accepting this article for publication, acknowledges that the United States Government retains a non-exclusive, paid-up, irrevocable, worldwide license to publish or reproduce the published form of this work, or allow others to do so, for United States Government purposes.

Nanoparticle Treated Stainless Steel Filters for Metal Vapor Sequestration

*Simona E. Hunyadi Murph,^{*1,2} George K. Larsen,¹ Paul Korinko,³ Kaitlin Coopersmith,¹ Ansley Summer¹ and Rebecca Lewis¹*

¹*National Security Directorate, Savannah River National Laboratory, Aiken, SC USA*

²*Department of Physics and Astronomy, The University of Georgia, Athens, GA, USA*

³*Energy Materials Directorate, Savannah River National Laboratory, Aiken, SC USA*

**Corresponding author, email address: Simona.Murph@srnl.doe.gov*

Phone: 1-803-646-6761, Fax: 1-803-646-6761

Abstract

The ability to sequester vapor phase radioactive compounds during industrial processes reduces the exposure of workers and the environment to dangerous radioactive materials. Nanomaterials have a lot of potential in this area because they typically demonstrate size and shape dependent properties with higher reactivity than bulk due to the increased surface area-to-volume ratio and quantum size effects. In this report, we developed a gold nanomaterial treated stainless steel filter (SSF) that can be efficiently used for zinc vapor sequestration. Without nanoparticle modification, stainless steel coupons do not react or alloy with Zn. Gold nanomaterials were grown onto various stainless steel filters using solution chemistry that is amenable to scaling up. Materials were characterized by electron microscopy, inductively coupled plasma mass spectroscopy (ICP-MS) and dynamic light scattering before and after exposure to zinc vapors. X-ray diffraction (XRD), High Resolution Transmission Electron Microscopy (HRTEM), Energy dispersive X-ray analysis (EDX) mapping and UV-Vis spectroscopy confirm the formation of gold-zinc alloys after Zn vapor exposure. The effect of surface topography on nanoparticle morphology, size and loading density were also investigated and stainless steel surface defects were found to have an impact on the AuNP growth.

Keywords: Zinc Vapor, Nanoparticles, Characterization, Sequestration

1. Introduction:

Radioactive materials pose a risk to the environment and all living organisms. One of the greatest problems associated with radioactive materials is the long-term storage, disposal, or transformation of the waste into a non-toxic form. Safe capture and disposal has proven to be a formidable task because of the long half-life, toxicity, and high energy emitted from radioactive waste. Currently, there are several ways in which nuclear waste is temporarily stored because a long term viable solution for nuclear waste disposal has not yet been agreed upon. [1] In order to avoid exposure to radioactive materials, one needs to develop effective sequestration technologies that (a) reduce potential dose to the environment and living organisms, (b) capture the radiological contaminant in an area that was designed for, and (c) can be disposed in a safe manner.

In the last few decades, nanomaterials have emerged as effective sequestering agents for a variety of analytes, including metals, gases, anticancer agents, and radioactive materials. [2-7] Nanomaterials exhibit unique properties due to their large surface area and quantum size effects [8-10]. Due to the larger fraction of atoms at the particle surface, nanoparticle based sequestering agents have been found to have a higher adsorption activity compared to conventional macroscale/bulk materials and the high surface area to volume ratio of nanoparticles typically leads to faster reaction kinetics and higher remediation capacities. [11, 12] The nature and the structure of the material can also affect the adsorption and oxidation/reduction processes, controlling the formation of adsorbed intermediates and the products.[9,13] Decreasing the particle size and manipulation of surface conditions and properties can boost the performance of the current sequestration technologies and reduce the material's cost. [9,13,14]

Additionally, nanomaterials surface chemistry can be easily tailored for targeted in situ sensing and remediation processes. [16,17] For example, surface functionalized polymer nanoparticles have been reported as selective sequestering materials of heavy metals.[2] Silica nanoparticles were also used for sequestration and luminescence detection of trivalent rare-earth ions (Dy^{3+} and Nd^{3+}) in solution.[3] Recent studies have shown that zero valent iron (ZVI) is an effective remediation agent for treating arsenic-laden,[4] halogenated hydrocarbons, [5] hexavalent chromium,[6] and other heavy metal species [7] in water, groundwater or drinking water. Nanoparticles have well defined structures and are often thermally and chemically stable in harsh environments. For example, calixarene-crown-6 derivatives with terminal carboxyl groups attached to nano-sized magneto ferritin molecules can sequester radioactive cesium (I) ions from aqueous solution. [18] These properties give nanoparticle based sequestering agents the potential for faster waste treatment technologies with the creation of less waste.

Among many classes of metallic nanoparticles developed in the last few decades, gold nanoparticles are among the most attractive materials. This is in part due to their surface plasmon resonance that can be tuned in the visible-near IR regions of the spectrum and can be exploited for sensing, sequestration and biological applications [8-10, 13, 14, 17]. Gold is also resistant to oxidation and corrosion. The ease of surface engineering with a variety of functional groups opens new doors toward exploring their outstanding mechanical, electrical and structural properties.[19] The ability to produce them by solution chemistry, which is amenable to scaling up, allows one to develop technologies and materials that enable new, low cost, effective and environmentally friendly solutions for industrial sequestration and remediation applications.

^{65}Zn is one of the twenty-five radioisotopes of zinc with a half-life of 244.26 days. ^{65}Zn , a positron (beta+) and gamma emitter constituent [20], is generated by the neutron-activation reaction of stable zinc (^{64}Zn) in nuclear reactors and can be found in the coolant of atomic power plants. [21] ^{65}Zn can be generated when gallium nuclei are bombarded with protons. [22] For example, a total of 457 mCi of ^{65}Zn was produced as a byproduct of ^{68}Ge processing. [23] ^{65}Zn , a radiological contaminant, is also generated during tritium extraction processes at Savannah River Site. [16, 24, 25] The radioisotope (65) of Zn has a wide range of applications, especially as a tracer in botany and agriculture. [26] A number of studies have investigated the toxicity of the emitter ^{65}Zn . It was found that once ^{65}Zn is taken into the body, it irradiates tissues with 1.1 MeV gamma-rays with a biological half-life of 400 days. [27] To minimize the potential for ^{65}Zn exposure, an effective methodology is needed to reduce the risk of radiation injury.

This paper describes a sequestration nanotechnology approach developed to capture and retain zinc vapors that contain the radioactive gamma emitting zinc and reduce potential dose to the worker. Specifically, gold nanoparticles were grown on stainless steel filters, namely wools and coupons, and their efficacy for zinc vapor capture and retention was evaluated. Gold nanomaterials were selected based on bulk thermodynamic properties that indicated they would form zinc compounds. Gold nanomaterials were produced by solution chemistry that can be scaled up to coat larger sized filters. Stainless steel was chosen as filter support because it does not react or alloy with Zn, and the Zn vapor does not condense to form deposits on the surface in appreciable quantities without nanoparticle modification. By using a passive substrate in the form of a stainless steel support, the sequestration properties of the Au nanoparticles can be more easily isolated and examined.

2. Experimental Section:

Gold nanoparticles were grown on Type 316L stainless steel filters (SSF), specifically wool (SSW) and coupons (SSC). SSW were nominally 50mm x 10mm diameter pads while SSC dimensions were 10cm x 2cm. Gold nanoparticles were prepared by a citrate reduction approach [ref] in the presence of the filter support. Specifically, $1.25 \times 10^{-4} \text{M Au}^{3+}$ was heated to boiling and 1 wt % sodium citrate solution was added. The boiling was continued until the solution turned ruby red, indicating the formation of gold nanoparticles. The resulting nanoparticles treated filters were purified by three steps washing in deionized water. The as-received stainless steel filter (control) was characterized using a Keyence VR 3000 profilometer and scanning electron microscopy (SEM). The grit blasting procedure was performed to create rough surfaces by exposing SSC to flowing alumina media for 7 seconds at 60 psi. The nanoparticle (NP) treated filters were characterized using scanning electron microscopy (SEM), energy dispersive X-ray analysis (EDX) and EDX elemental mapping to elucidate their morphology, topography and composition. The NP's optical properties were evaluated by UV-Vis spectroscopy. The adhesion of the NP deposit to the filters was tested using an ultrasonic cleaner and an aqueous solution using fixed time increments. The resulting aliquot solutions were analyzed by inductively coupled plasma atomic emission spectroscopy (ICP-AES) to determine the amount of the deposit that was removed. ICP-AES experiments were also performed to quantify the amount of metals present on the support (Zn, Au). X-ray powder diffraction (XRD) and high resolution transmission electron microscopy analysis were used for phase identification of a crystalline material upon Zn vapor exposure. Samples were exposed to zinc vapor from a high vacuum thermal deposition apparatus. The system is comprised of an all metal seals and Conflat™ flanges. The samples were supported on perforated metal with a stack of up to four samples being exposed during one exposure. A bronze pellet was included in the exposure as an experimental control and to verify that the deposition apparatus operated correctly. The zinc vaporization and filter temperature conditions, 350°C for both and an initial vacuum pressure of approximately 5×10^{-6} Torr, used were consistent with previous work [16].

3. Results and Discussions

3.1. Nanoparticle's Preparation and Growth Mechanism

Gold nanoparticles were grown on stainless steel filters supports through a reduction process, namely the Turkevich approach. It was found that the size and density of nanoparticle's formation depends on many factors such as the reaction temperature, duration of the process as well as the nature of solid supports and their surface energy. The desired Nps size and loading density was controlled and tailored by careful selection of experimental parameters as reported. [8-11, 13, 14, 16, 17] The preparation procedure used to fabricate gold nanoparticles is based on a solution chemistry approach that can be easily scaled up. Gold nanoparticles produced are stable for years and can be easily deployed. They do not require expensive instrumentation and can be easily functionalized for further applications.

Growth of the gold nanoparticles (Au Nps) onto stainless steel filters (SSF), wools (SSW) and coupons (SSC) was monitored by SEM. Representative SEM images of Au nanoparticles deposited on SSC and SSW filters are shown in Figure 1.

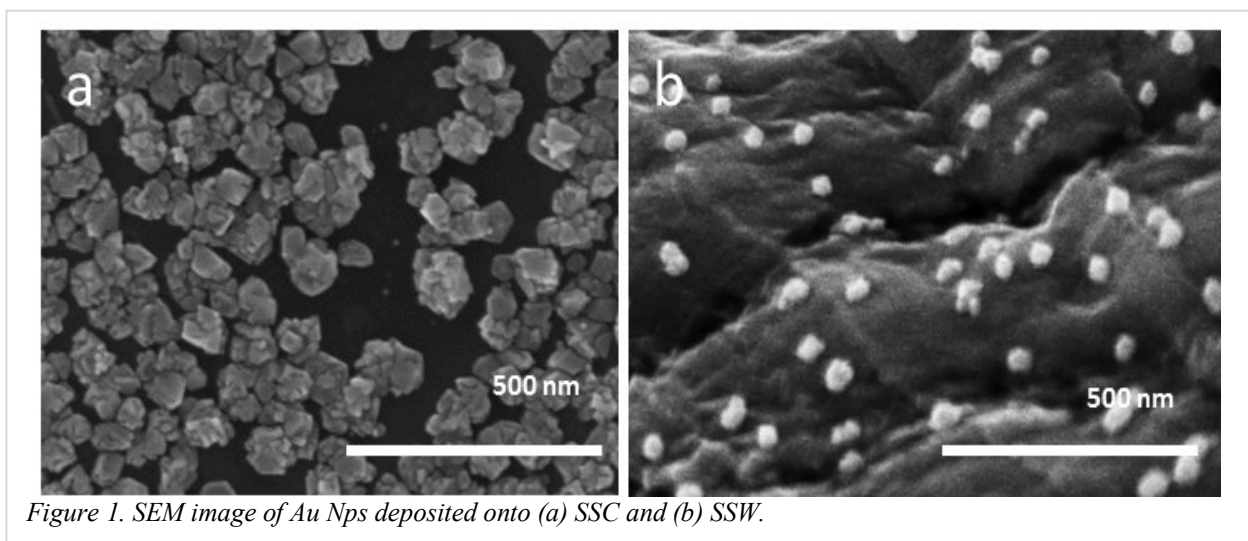


Figure 1. SEM image of Au Nps deposited onto (a) SSC and (b) SSW.

SEM images show that the nanoparticles are distributed over the entire wire surface. Even though identical experimental parameters were used during Au Nps preparation on SSC and SSW, slightly different morphologies (size, shape, pitch) were produced. The local topography of the nanoparticles deposited onto SSC is significantly different than those produced onto SSW. Particle-size distribution determined on SSW by measuring Au nanoparticles on scanning electron micrographs was found to be 26 ± 2 nm in diameter with a relative spacing of 100 nm. Selected areas also show multiplet-type cluster nanoparticles with an average diameter of 78 nm. Au Nps dimensions on the SSC were on average 34 ± 5 nm in diameter with ≈ 10 nm average spacings between particles. Survey images over large filter's areas reveal that, while Au nanoparticles were well dispersed on SSC, the nanoparticles appear as truncated structures with straight edges connected by jagged corners.

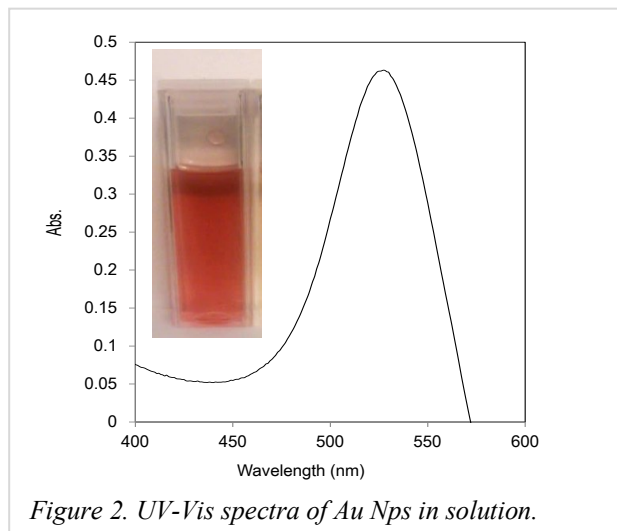


Figure 2. UV-Vis spectra of Au Nps in solution.

The nanoparticle's optical properties were evaluated by UV-Vis spectroscopy (Figure 2). In deionized water, the gold nanoparticles display the characteristic peak at around 525 nm that corresponds to the plasmon band (collective oscillation of electrons) for spherical gold nanoparticles of approximately 20 nm in agreement with published research. [8-11, 13, 14, 16, 17]

3.2. Filters Selection

Stainless steel filters were chosen in this study because they do not react or alloy with Zn, and the vapor does not condense to form deposits on the surface in appreciable quantities without nanoparticle modification. By using a passive substrate, the sequestration capacities of the Au nanoparticles can be isolated and examined accurately.

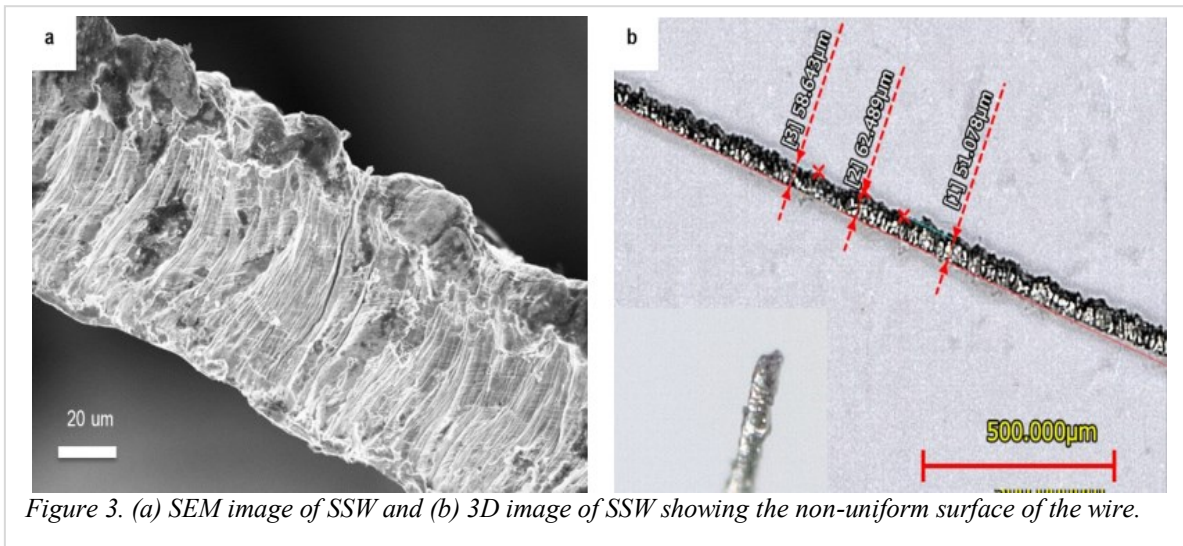
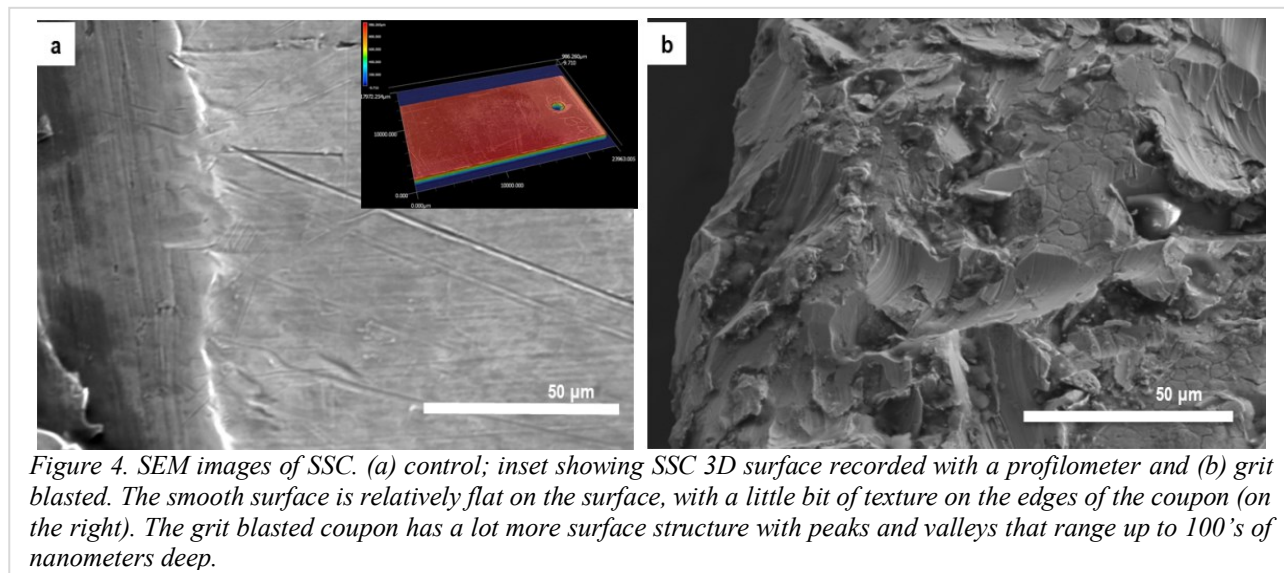


Figure 3. (a) SEM image of SSW and (b) 3D image of SSW showing the non-uniform surface of the wire.

The presence of distinct well-defined steps, defects and boundaries are powerful predictors for nanoparticle's growth evolution and location. [28] The defect-like surfaces and boundaries on supports play a crucial role on the nucleation and growth of metallic nanoparticles [10, 13]. Scanning electron microscopy studies were conducted to elucidate SSF's topography before modification with Au Nps (Figure 3).

A thorough investigation of the SSW surface reveals that the wires exhibit a multitude of valleys, steps and crevices while the SSC display a smooth surface. The SS filters were also examined optically using a 3D profilometer (Figure 2). The nominal diameter of the wires is 50 μ m. The SSW wire has a surface roughness of 5.44 RA and nanofeatures of 20-50 nm. As a result, an investigation was undertaken to evaluate the importance of defect

like features (valleys, crevices) on nanoparticle's deposition. A grit blasting procedure was developed on SSC to increase the surface roughness of the stainless steel coupons prior to coating with nanoparticles to facilitate uniform experimental interrogation and to maintain consistency across experiments. SEM images (Figure 4) show that grit blasting leads to nano-features of 100-600 nm.



The number of Au nanoparticles formed on the SSF surface is intimately connected with the number of defects presents on the surface and experimental parameters (temperature, pH, concentration, reaction time) used during the preparation procedure. On a highly defective surface, clusters nucleate and grow at point defects on the terraces. The Au Nps nucleation and growth mechanism follows several steps: (a) reduction of the gold precursor and formation of nucleation centers clusters, (b) formation of seed particles, (c) slow and fast growth of Au nanoparticles. [8-10, 14, 19, 29-31] A closer inspection of the SSW surface shows that Au Nps are distributed over the entire SSF surface with more than 90% presence on the defects on terraces. Previous studies reported by Goodman's group [32] shows that, on a low-defect surface, Au clusters nucleate and grow at line defects with metal deposition at room temperature, whereas deposition at high temperature leads to cluster decoration primarily at step edges. During Au nanoparticle's deposition process, it was found that the surface's topography is critical for the Zn vapor sequestration process. Significant differences were observed on the Au morphologies produced on SSC vs. SSW. It was discovered that support's surface condition, topography or roughness leads to different Au Nps morphologies and surface loading, e.g. surface densities.

Upon Au Nps deposition, a less dense nanoparticle population was recorded on the grit blasted SSC compared with the smooth SSC (Figure 5), from $\approx 91\%$ to $\approx 67\%$. The nanoparticles are however formed as discrete particulates with dimensions of 57 ± 18 nm on the grit blasted surfaces. A rough surface was also beneficial to the metallic components (Au and Zn) adhesion and stability. The presence of surface defects and roughness dramatically enhances the stability and retention of the metallic components involved, namely Au nanoparticles and Zn metal vapors (data not shown).

3.3. Zinc Vapor Sequestration

Individual samples of Au treated SSW and SSC were exposed to zinc vapor using previously established conditions. [16] The typical thermal and pressure profiles observed are indicated in Figure 6. The filter reaches the target temperature before the zinc is heated so that the zinc vapor can be captured at the desired temperature. Due to the extensive history of bronze exposures, a bronze pellet was included in the experiment to verify that the zinc vapor was sufficient to deposit on all the samples. The zinc vaporization and filter temperature conditions, 350°C for both and an initial vacuum pressure of at least 5×10^{-6} Torr is shown in Figure 6.

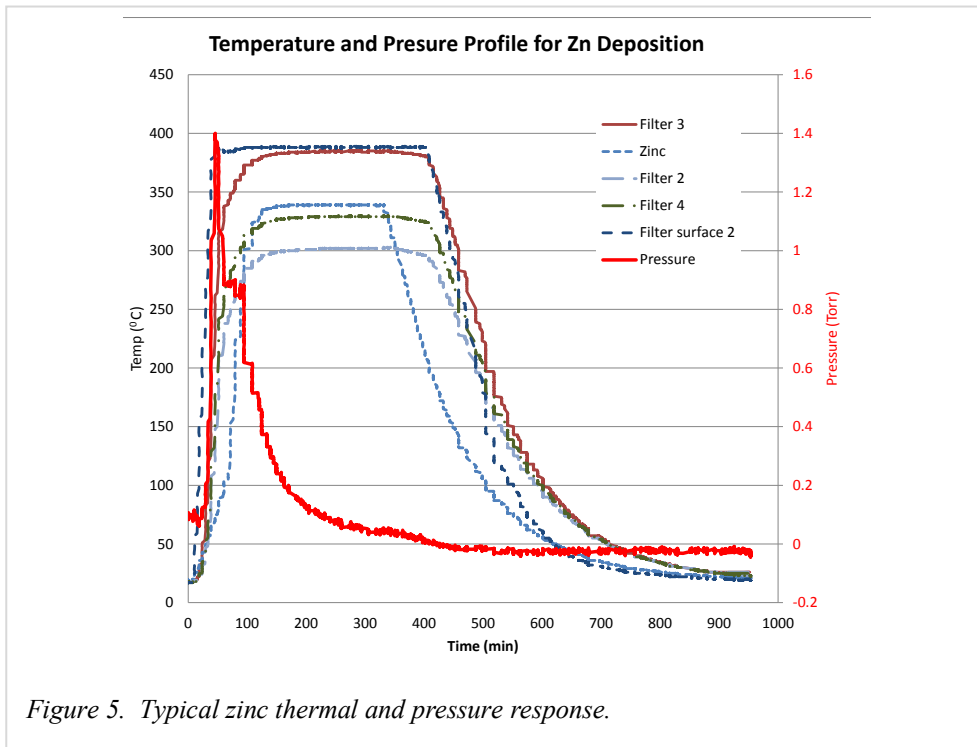


Figure 5. Typical zinc thermal and pressure response.

Visual examination of the bare and nanomaterial treated SS-W exposed to zinc did not reveal any change in color as is typically observed for the bronze pellets which are initially orange (bronze) colored and change to a golden tint (brass) after zinc alloying, as shown in Figure 7 for SSF and bronze pellets, respectively. There may be a slight change in the sheen of the SS-W indicated by the photos, but this difference may simply be due to changes in lighting between the photos. A significant color change was observed on the SSC before and after Zn exposure. A yellow color appears purple-like upon Zn exposure demonstrating the Zn sequestration progression.

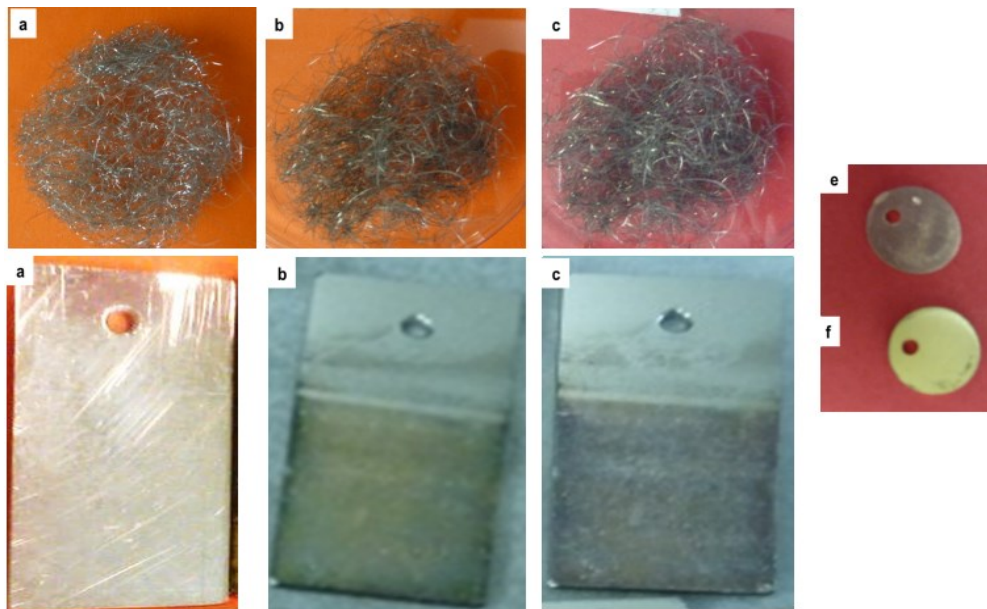


Figure 7. Photographs of SSF. Top row: SSW (a) control, (b) nanoparticle treated before Zn exposure, (c) after zinc exposure and typical bronze pellets before (e) and (f) after zinc exposure. Bottom row: SSC (a) control, (b) nanoparticle treated before Zn exposure, (c) after zinc exposure.

Electron dispersive X-ray microanalysis (EDX) of Au Nps treated filters was performed to evaluate chemical composition before and after Zn vapor capture (Figure 8). These results confirmed clearly that the nanoparticles' treated SSW filters are effective at capturing Zn vapors. The untreated-control SSF (no Au nanoparticles) did not capture any Zn demonstrating that the SS control remained inert upon Zn exposure. This is the first indication that gold nanoparticles are the sequestering agent for Zn vapors.

Scanning electron microscopy studies were conducted to elucidate the morphological changes of filters before and after Zn exposure. Zn deposits can be

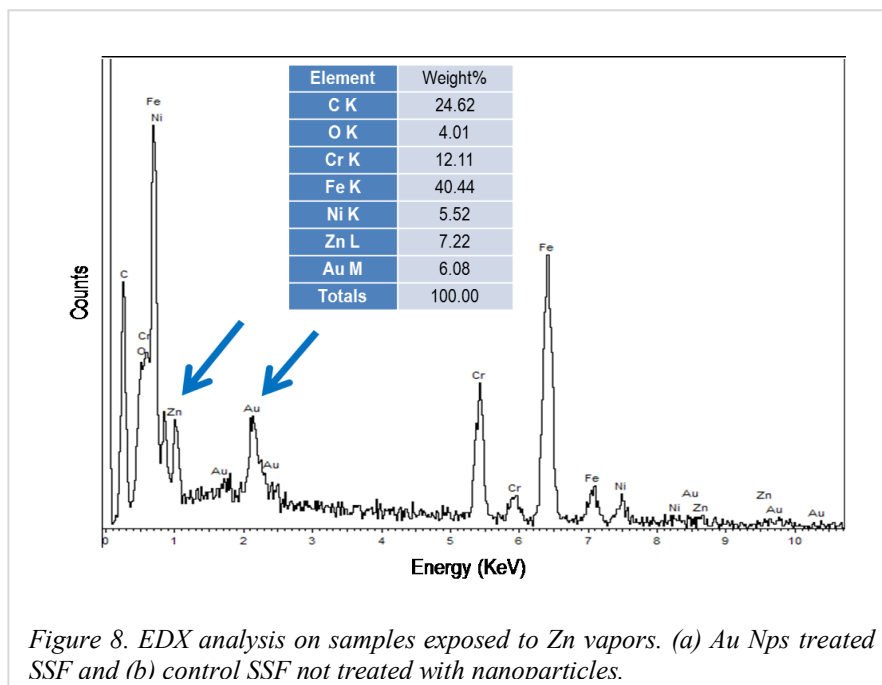


Figure 8. EDX analysis on samples exposed to Zn vapors. (a) Au Nps treated SSF and (b) control SSF not treated with nanoparticles.

easily observed after Zn vapor exposure on all Au Nps treated SSF (Figure 9). All deposits seem to have increased in size incrementally. The Zn content ranged from ~2.5 to ~7 wt % and was determined based on EDX analysis. Table 1 shows the nanoparticle sizes before zinc deposition and after zinc deposition on SSW. For the Au Nps before zinc exposure, discrete particles having an average size of around 26 nm and nanoparticle clusters having an average size of around 78 nm were observed. After zinc exposure, the nanoparticles increased in size. For instance,

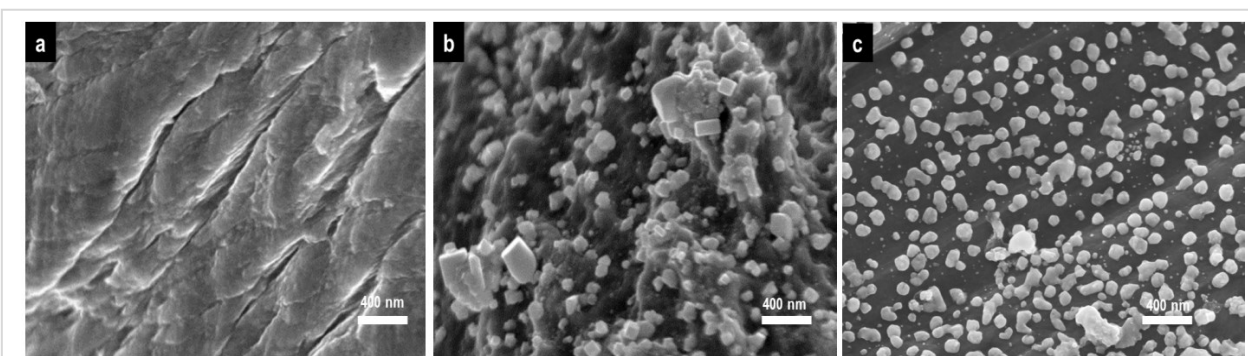


Figure 9. SEM images of filters exposed to Zn vapors (a) control SSF (not treated with Au Nps and exposed to Zn), (b) Au NPs treated SSW and (c) Au NPs treated grit blasted SSC.

the average of the nanoparticles was approximately 32 nm, while nanoparticle clusters had a multimodal distribution (e.g., average sizes of 85 nm, 125 nm, 239 nm and 371 nm). The results are indicated in Table 1. SSC modified with Au nanoparticles shows nanoparticles sintering effects after exposure to Zn vapors. This is not surprising, since, the chemical reactivity of the surface metal atoms on these nanoparticles is closely related to their chemical potential. Specifically, the higher their chemical potential, the more strongly they bond to small adsorbates, which could be Zn vapor or Nps found in the close proximity. Also, when the metal atoms are in a nanoparticle with higher chemical potential, they experience a larger thermodynamic driving force to sinter. Sintering may be beneficial due to the increase adhesion properties which may keep the zinc deposits attached to the supports.

Table 1. Average Sizes Before and After Zinc Exposure on SSW

Nanoparticle on SSW	Average Size Before Zinc Exposure (nm)	Average Size After Zinc Exposure (nm)
Au	26	32
	78	85
	-	125
	-	239
	-	371

When Au Nps treated SSC were evaluated as zinc getters, a significant mass increase (easily measured on an analytical scale balance) of approximately $\approx 0.1\text{mg}$ of Zn (surface area 1.6cm^2) was collected on the filter support, demonstrating once again that the nanoparticles are effective Zn getter materials.

A closer investigation of the SSF exposed to zinc shows that Zn deposits are being “captured” by the Au nanoparticles (Figure 10a). This could be due to the (a) crystalline migration and/or (b) atom migration on the support. [33] It is certainly possible that, at $350\text{ }^\circ\text{C}$, the metal crystallites could migrate, collide, and coalesce on the support surface. Additionally, as described by Porter and Easterling, metal atoms migrate from one crystallite to another in a manner consistent with reduction of surface energy as making big crystallite bigger and small crystallites smaller; basically, larger particles are growing at the expense of the small ones. [34]

EDX mapping was also performed to elucidate the location of the elements of interest; Au and Zn. An image analysis software program (ImageJ) has been evaluated for characterizing the electron micrographs of the deposits (data not shown). A thorough analysis collected on hundreds of samples indicates an increase in nanoparticle size after Zn exposure ($\sim 13\text{-}15\%$ increase in surface area).

For a rigorous metal quantitation, inductively coupled plasma mass spectroscopy (ICP-MS) was performed on all supports before and after Zn exposure (Figure 11). Zn is partially removed from all coupons after sonication experiments but most of the original Au Nps are retained on the SSF supports. In order to elucidate the nanoparticulate size distribution profiles of all sonicated solution (from the parent Au Nps treated coupons and Au Nps treated exposed to Zn coupons), dynamic light scattering (DLS) experiments were employed. Data collected on SSW shows that different size particulate population sizes were removed from the supports. Larger particles were released at the beginning of the sonication experiments with the smallest particulates being released after 60 minutes. However, in the case of SSC, uniform particulate population were produced with an almost identical particulate sizes being removed after 10, 30 or 60 min sonication experiments. After sonication of the Au Nps treated coupons and analyzed by SEM, a significant amount of nanoparticles remains onto the solid support even after 60 minutes sonication. The larger particles (zinc deposits), however, are being removed throughout the sonication experiments. This demonstrates that oversaturation of the Au nanoparticle getters with Zn was occurring. This hypothesis was tested and demonstrated by reducing the exposure time to a reduced flux of zinc vapor and will be published at a later date.

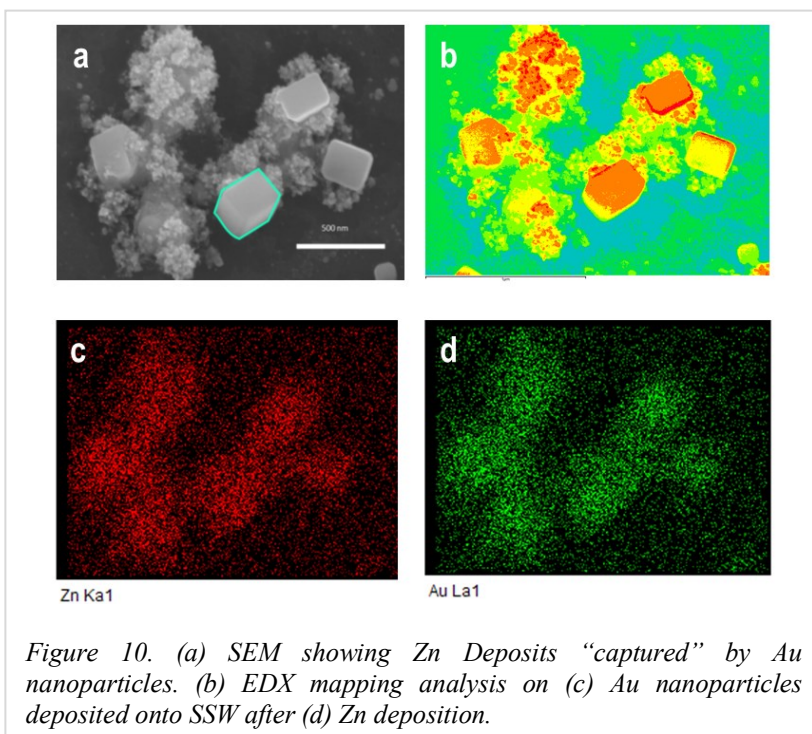


Figure 10. (a) SEM showing Zn Deposits “captured” by Au nanoparticles. (b) EDX mapping analysis on (c) Au nanoparticles deposited onto SSW after (d) Zn deposition.

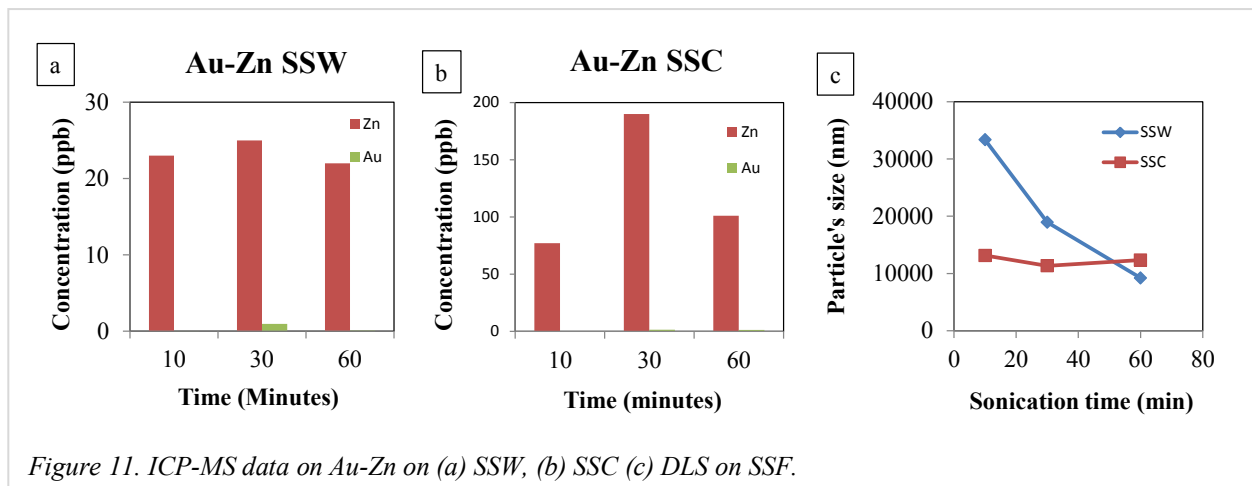


Figure 11. ICP-MS data on Au-Zn on (a) SSW, (b) SSC (c) DLS on SSF.

The optical properties of the particulates removed from the supports were evaluated by UV-Vis spectroscopy (Figure 12). In deionized water, the Au Nps removed from the coupons display a peak at around 550 nm that corresponds to the plasmon band (collective oscillation of electrons) for spherical gold nanoparticles [8-10]. This shows that Au deposited on the SSF are $\approx 30\%$ larger in diameter than Au Nps in solution. The UV-Vis spectra of the Au Nps exposed to Zn nanostructures differ from the Au Nps. A red shift and a broader peak of the original Au NPs plasmon band, originally at approximately 550 nm, was observed after Zn exposure to 550-650nm. This confirms the formation of alloy gold-zinc structures.

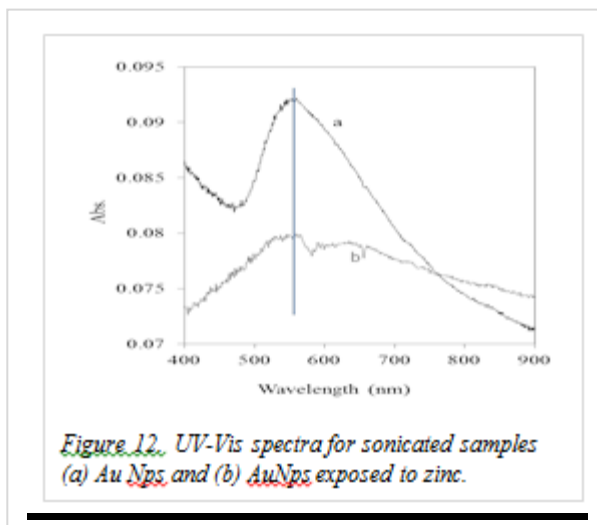


Figure 12. UV-Vis spectra for sonicated samples (a) Au Nps and (b) AuNps exposed to zinc.

In order to determine whether or not the AuNps capture Zn through adsorption or alloying, X-ray diffraction (XRD) analysis was performed. The XRD spectra are shown in Figure 13. It can be seen that the stainless steel coupons (SSC) produce three strong peaks, which agree with literature values for stainless steel. Au Nps coated on SSCs do have a small additional peak, which agrees the diffraction peak of Au (111). After exposure

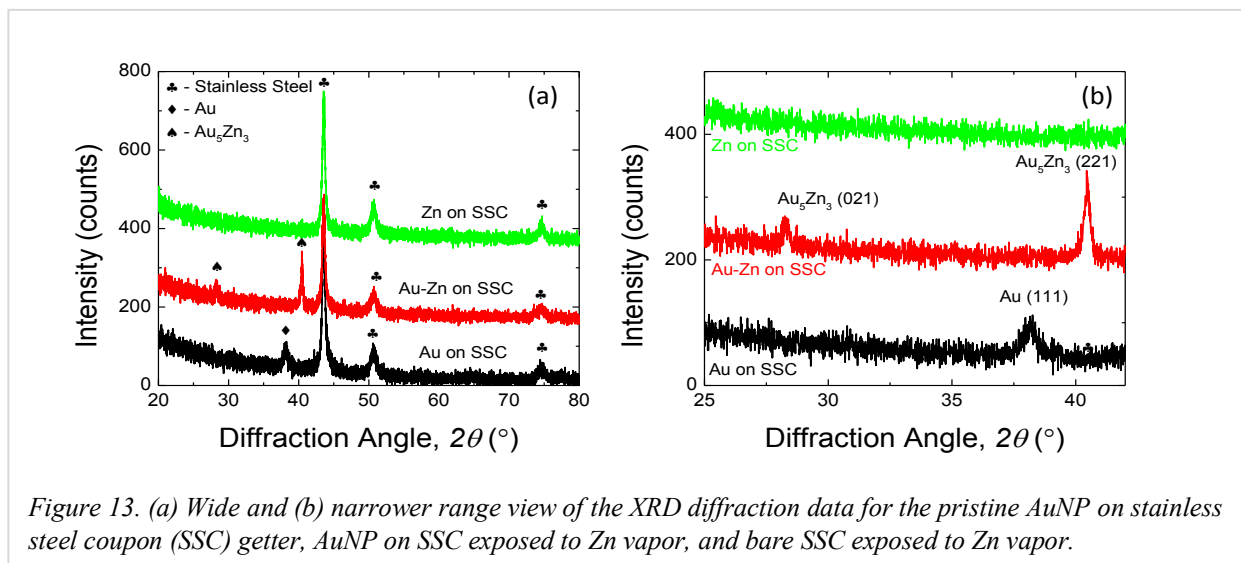


Figure 13. (a) Wide and (b) narrower range view of the XRD diffraction data for the pristine AuNP on stainless steel coupon (SSC) getter, AuNP on SSC exposed to Zn vapor, and bare SSC exposed to Zn vapor.

to Zn vapor, the Au (111) peak disappears, and two new peaks emerge that coincide with Au_5Zn_3 alloy. However, these peaks are somewhat shifted to higher angles, suggesting tensile stress in the lattice. The SSC exposed to Zn only exhibits diffraction peaks associated with stainless steel. This is an important result, as the sequestration capability of the AuNPs and the adhesion of the Zn atoms is directly related to the alloying process. According to the Au-Zn binary phase diagram, the Au_5Zn_3 phase results from a peritectoid transformation ($\alpha_1 + \beta' \rightarrow \text{Au}_5\text{Zn}_3$) at 300 °C, which, in this experimental case, follows from a eutectoid transformation ($\text{Au} \rightarrow \alpha_1 + \beta'$) that typically occurs at 400 °C for bulk materials. Thus, this suggests that the Au nanoparticle deposits alloy at lower temperatures than traditional bulk Au. Similar size-effects in the alloying and melting temperatures of nanoparticles have been observed before, and such effects are beneficial for sequestration by reducing the amount of thermal energy necessary for a phase transition.

A small portion of the nanoparticles are removed during a sonication process and these allow for further analysis of the getter properties. The sonicated nanoparticles have been characterized by SEM, EDX, EDX mapping, UV-Vis spectroscopy and HRTEM. These studies in conjunction with the XRD analysis show that Zn is prevalent on and/or within the getter materials at a ratio somewhat larger than that indicated by alloying (Au_5Zn_3 , $\text{Zn}/\text{Au} = 0.6$). ICP-MS shows Zn as overwhelmingly the most prevalent metal in the sonicated solution. The HRTEM imaging supports these findings in showing the sonicated nanoparticles to be AuZn alloy (Figure 14). The lattice fringes for Au {111} with $d = 2.3 \text{ \AA}$ changed to $d = 2.48 \text{ \AA}$ after Zn deposition. These results confirm the alloying effect is occurring.

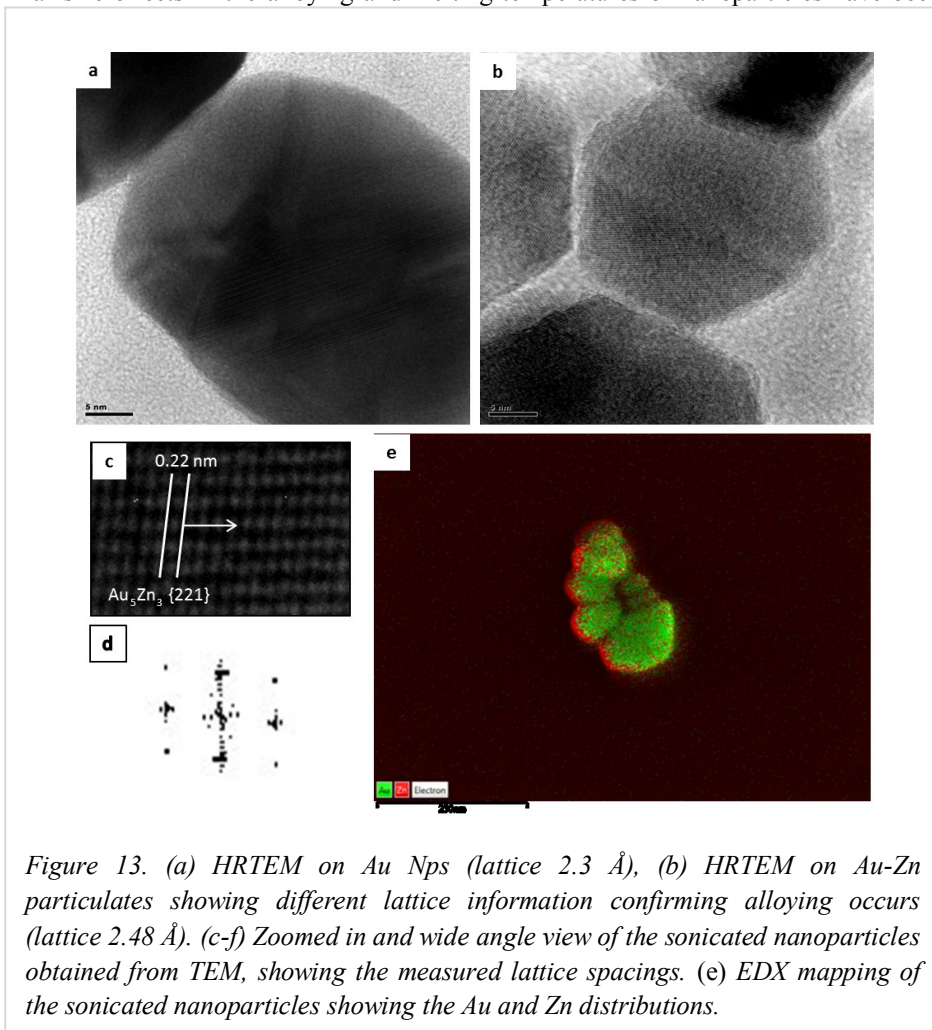


Figure 13. (a) HRTEM on Au Nps (lattice 2.3 Å), (b) HRTEM on Au-Zn particulates showing different lattice information confirming alloying occurs (lattice 2.48 Å). (c-f) Zoomed in and wide angle view of the sonicated nanoparticles obtained from TEM, showing the measured lattice spacings. (e) EDX mapping of the sonicated nanoparticles showing the Au and Zn distributions.

4. Conclusions:

We reported the successful capture of Zn vapors using stainless steel filters functionalized with gold nanoparticles. AuNP growth was influenced by the surface topology of the stainless steel filters and experimental parameters. Growth on the rougher SSCs led to smaller nanoparticles that were further apart compared to those grown on the smoother SSCs. Grit blasting the SSCs prior to gold nanoparticle growth led to a lower distribution of AuNPs, but the particles were more discrete. The differences between the distribution, morphology and size of the AuNPs on the different SSFs are due to the presence of more defect sites on the wires and grit blasted coupons that affect the mechanism of AuNP deposition.

The capture and retention of Zn vapor on AuNP treated SSWs occurred via an alloying mechanism. XRD and HRTEM confirmed the formation of Au_5Zn_3 alloys and SEM confirmed an increase in the nanoparticulate size on

the stainless steel support after Zn adsorption. The AuNPs were more reactive than bulk Au since the alloys were formed at lower temperatures than expected for bulk Au. The lack of Zn adsorption on SSF's without AuNPs demonstrates that the AuNPs are the sequestering agents for the Zn vapor. This investigation demonstrated the ability of nanoparticles to impart reactivity toward metal vapor sequestration on otherwise unreactive supports. This method can be applied to capture other metal vapors to reduce exposure to workers and the environment during waste treatment and remediation.

Acknowledgements

The authors would like to acknowledge Savannah River Tritium Enterprise for providing funding for this work under contract DE-AC09-08SR22470.

References

1. <http://www.energy.gov/ne/nuclear-waste-challenge>
2. C. A. Bell, S. V. Smith, M. R. Whittaker, A. K. Whittaker, L. R. Gahan, and M. J. Monteiro, *Adv. Mater.* 18, 582 (2006).
3. S. D. I Topel, E. P. Legaria, C. Tiseanu, J. Rocha, J. M. Nedelec, V. G. Kessler, and G. A. Seisenbaeva, *J Nanopart Res.* 16, 2783 (2014).
4. W. Yan, M. A. V. Ramos, B. E. Koel, and W. X. Zhang, *J. Phys. Chem. C.* 116, 5303 (2012).
5. S. M. Ponder, J. G. Darab, T. E. Mallouk, *Environ. Sci. Technol.* 34, 2564 (2000).
6. Y. Q. Liu, H. Choi, D. Dionysiou, G. V. Lowry, *Chem. Mater.* 17, 5315 (2005).
7. X. Q. Li, W. X. Zhang, *J. Phys. Chem. C.* 111, 6939 (2007).
8. S. E. Hunyadi Murph, K. Heroux, C. Turick, and D. Thomas, *Nanomaterials and Nanostructures 4*, ed. J.N. Govil, (Houston: Studium Press LLC, 2012), vol 4.
9. S. E. Hunyadi Murph, S. Serkiz, E. Fox, H. Colon-Mercado, L. Sexton, and M. Siegfried, *Fluorine-Related Nanoscience with Energy Applications 1064*, eds. D. J. Nelson, C. N. Brammer (London: Oxford University Press, 2011), pp. 127-163.
10. G. Larsen, W. Farr, and S. E. Hunyadi Murph, *J. Phys. Chem. C.* 120, 15162 (2016).
11. X. Li, *Langmuir* 22, 4638 (2006).
12. H. Wang, *Dalton Trans.* 40, 559 (2011)
13. S. E. Hunyadi Murph, and C. J. Murphy, *J. Nanoparticle Res.* 15, 1607 (2013).
14. S. E. Hunyadi Murph, C. J. Murphy, H. Colon-Mercado, R. Torres, K. Heroux, E. Fox, L. Thompson, and R. Haasch, *J. Nanoparticle Res.* 13, 6347 (2011).
15. M. Kar, *Langmuir* 27, 12124 (2011).
16. P. Korinko, and S. E. Hunyadi Murph, Development and Characterization of Nanomaterials for Zinc Vapor Capture, Proceedings: Characterization of Minerals, Metals and Materials, 2015 TMS Annual Meeting & Exhibition.
17. C. J. Murphy, A. M. Gole, S. E. Hunyadi, J. W. Stone, P. N. Sisco, A. Alkilany, B.E. Kinard, and P. Hankins, *Chem. Comm.* 4, 554 (2008).
18. I. Urban, N. M. Ratcliffe, J. R. Duffield, G. R. Elderb and D. Pattona, *Chem. Commun.* 46, 4583 (2010).
19. C. J. Murphy, T. K. Sau, A. M. Gole, C. J. Orendorff, J. Gao, L. Gou, S. E. Hunyadi, and T. Li, *J. Phys. Chem. B* 109, 13857 (2005).
20. P. Etcheverry, J. C. Wallingford, D. D. Miller, and R. P. Glahn, *J. Agric. Food Chem.*, 50, 6287 (2002).
21. I. Sato, and S. J. Tsuda, *Vet. Med. Sci.* 70, 213 (2008).
22. J. M. Fitzsimmons, and L. Mausner, *Appl. Radiat. Isot.* 101, 60 (2015).
23. D. G. Medvedev, L. F. Mausner, G. E. Meinken, and S. O. Kurzak, *J. Radioanal. Nucl. Chem.* 280, 137 (2009).
24. P. S. Korinko and M. H. Tosten, *JFAP* 13, 389 (2013).
25. P. S. Korinko, A. J. Duncan and K. J. Stoner, *JFAP* 14, 113 (2014).
26. G. Luccioni, G. Cicoria, D. Pancaldi, C. Malizia, and M. Marengo, *Appl. Radiat. Isot.* 70 1590 (2012).
27. I. Sato and S. Tsuda, *J. Vet. Med. Sci.* 7, 213 (2008).

28. S. E. Hunyadi Murph, C. J. Murphy, A. Leach, and K. Gall, *Cryst. Growth Des.* 15, 1968 (2015).
29. J. R. Polte, T. T. Ahner, F. Delissen, S. Sokolov, F. Emmerling, A. F. Thünemann, and R. Kraehnert, *J. Am. Chem. Soc.* 132, 1296 (2010).
30. J. Polte, *J. Cryst. Eng. Comm* 17, 6809 (2015).
31. M. Wuithschick, A. Birnbaum, S. Witte, M. Sztucki, U. Vainio, N. Pinna, K. Rademann, F. Emmerling, R. Kraehnert, and J. R. Polte, *ACS Nano* 9, 7052 (2015).
32. B. K. Min, W. T. Wallace, A. K. Santra, and D. W. Goodman *J. Phys. Chem. B* 108, 16339 (2004).
33. Z. Ma and S. Dai Heterogeneous Gold Catalysts and Catalysis, CHAPTER 1 : Stabilizing Gold Nanoparticles by Solid Supports 2014, pp. 1-26
34. D. A. Porter, and K. E. Easterling, *Phase Transformations in Metals and Alloys*, (London: Chapman & Hall, 1981)